Agricultural and Forest Meteorology 307 (2021) 108481

Contents lists available at ScienceDirect

Agricultural and Forest Meteorology

journal homepage: www.elsevier.com/locate/agrformet

Linking vegetation spectral reflectance with ecosystem carbon phenology in a temperate salt marsh

Andrew C. Hill, Alma Vázquez-Lule, Rodrigo Vargas *

Department of Plant & Soil Sciences, University of Delaware, 531 South College Ave., 152 Townsend Hall, Newark, DE 19716, USA

ARTICLE INFO

Keywords:
Ecosystem phenology
Vegetation indices
Phenocamera
Near-surface sensing
Remote sensing, NEP

ABSTRACT

Salt marshes constitute an important terrestrial-aquatic interface that remains underrepresented in Earth System Models due to constraining biophysical controls and spatially limited land cover. One promising approach to improve representativeness is the application of proximal remote sensing to generate phenological information, yet we lack detailed knowledge on how proximal sensors and indices perform within these ecosystems. We use measurements of net ecosystem productivity (NEP) from eddy covariance (EC) and derive ecologically-relevant phenology parameters (i.e., phenoperiods) to use as carbon phenology benchmarks. These benchmarks are compared against vegetation indices and spectral bands derived from spaceborne (i.e., MODIS) or common proximal sensors (i.e., phenocam and spectral reflectance sensors; SRS).

Phenocam derived indices, which exclude infrared wavelengths (i.e., vegetation contrast index; VCI and greenness chromatic coordinate; GCC), aligned closely with NEP benchmarks and provided best predictions of carbon sink season length (within 1–6 days of benchmark). Although isolating infrared from vegetation (NIRv) offered improvements, other indices utilizing infrared bands (i.e., normalized difference vegetation index; NDVI and enhanced vegetation index; EVI) primarily underestimated season start dates (5–30 days prior to benchmark) while overestimating season end dates (7–47 days after benchmark). These discrepancies are greatest for indices derived from MODIS and SRS sensors, which have narrower full width half maximum spectral bandwidths and sharper orientation angles. The phenocam (VCI and GCC) provides the most accurate phenology parameters while offering near-infrared (NIR) response which can generate additional information on seasonal changes in canopy structure and function.

The distinctive characteristics of the salt marsh environment and vegetation properties including standing dead biomass can introduce interpretation challenges for commonly used vegetation indices (NDVI, EVI). Incorporating information from proximal sensors utilizing only visible wavelengths (VCI, GCC) or isolating the near-infrared reflectance of vegetation (NIRv) offers improvements for studying carbon phenology within salt marshes.

1. Introduction

Remote sensing offers a valuable resource for parameterizing ecological models and provides a tool for monitoring changes in vegetation (i.e., phenology). Phenology provides a means to observe how changes in spectral reflectance oscillate with plant photosynthesis or respiration and more holistically, ecosystem carbon exchange (i.e., carbon phenology) (Piao et al., 2019; Richardson et al., 2013). There are increasing efforts to link vegetation reflectance and carbon dynamics at the ecosystem-scale across EC study sites (Gamon, 2015; Maleki et al., 2020) and couple this information with global terrestrial carbon models (Yuan et al., 2010). Unfortunately, there are limitations for spaceborne sensing applications within confined areas or limited landcovers (Helman, 2018; Hmimina et al., 2013). In particular, there are challenges for coastal ecosystems where geographies are bound by unique biophysical conditions occurring within the aquatic-terrestrial interface (Ward et al., 2020). The adoption of *in situ* near-surface remote sensing (i.e., proximal sensing) which provides complementary information and continuous validation for spaceborne applications offers important improvements. Incorporating proximal sensing to observe and track phenological changes via spectral reflectance may benefit representation of coastal ecosystems in global carbon models, yet we lack knowledge on which

* Corresponding author.
E-mail address: rvargas@udel.edu (R. Vargas).

https://doi.org/10.1016/j.agrformet.2021.108481
Received 9 December 2020; Received in revised form 12 May 2021; Accepted 14 May 2021
Available online 6 June 2021

proximal sensors and associated vegetation indices perform best within this specific environment. Consequently, there is a need to test the performance of common vegetation indices derived from spaceborne and proximal sensors to track daily carbon phenology and predict phenoperiod transition dates.

This study focuses on salt marshes as they are important components of coastal ecosystems and the carbon cycle (McLeod et al., 2011). Salt marsh grasses provide high productivity and the unique physical environment enables long-term storage of carbon within anoxic sediments (Barbier et al., 2011; Himes-Cornell et al., 2018; Seyfferth et al., 2020). Salt marshes also have patchy distributions and occupy less than 1% of terrestrial land surface (5.5 million ha), which generates challenges for spaceborne remote sensing (McOwen et al., 2017). Earth System Models (ESMs) reliant on common spaceborne data streams either omit or misclassify these environments (Zhu et al., 2016; Forkel et al., 2015; Meier et al., 2018), and there remains a need for better inclusion of aquatic interfaces (Vázquez-Lule et al., 2019; Ward et al., 2020). This lack of proper representation introduces uncertainties in model projections as ecological processes and drivers are different within salt-marsh environments due to specialized vegetation characteristics and biophysical conditions (Forbrich and Giblin, 2015; Weston et al., 2014).

Although studies have examined phenology using spaceborne data in salt marshes (Mo et al., 2015; Ghosh and Mishra, 2017), there remains challenges for properly representing carbon phenology in these ecosystems. Recent studies have examined phenological spatial heterogeneity within marshes using phenocams (O'Connell et al., 2020) and compared phenology metrics between high and medium resolution satellites while incorporating phenocam data (Dronova et al., 2021), albeit the focus was on freshwater marshes. Advancements have also been made at the continental scale where ecological models have been coupled with spaceborne data to estimate productivity of coastal wetlands (Feagin et al., 2020). We highlight that accurate phenology information is essential for both interannual comparisons within and between sites (e.g., differences in phenoperiod transition dates) and for higher frequency intra-annual monitoring (e.g., assessing tidal effects on ecosystem productivity). Improving remote sensing applications to characterize land atmosphere interactions in these ecosystems is also important for accurate monitoring and determining sequestration potentials to support preservation and restoration initiatives while providing quantitative information for local carbon markets (Sapkota and White, 2020; Pham et al., 2019).

Phenology provides a firm framework for studying change in biological processes affecting ecosystem carbon dynamics. Seasonal activation of these processes is closely linked to rates of mass and energy transfer and thus plays a key role in carbon cycle regulation. Linking spaceborne and proximal sensing information of plant phenology (based on spectral reflectance indices) with physiological plant processes (i.e., photosynthesis) has become a useful application for studying environmental change (Richardson et al., 2013). These advances are driven in part by increased availability and use of proximal sensors which includes narrow-band spectral reflectance sensors (SRS) (e.g., NDVI, photochemical reflectance index; PRI) (Gamon et al., 2015; Garbulsky et al., 2011) and visible-infrared enabled security cameras (phenocams; Petach et al., 2014; Richardson et al., 2009; Sonnentag et al., 2012), which have provided unprecedented information to validate and calibrate spaceborne approaches. Proximal sensors provide multi-temporal information which enables site-level integration with EC measurements (i.e., technique to measure exchange of mass and energy between the land surface and atmosphere) (Balzarolo et al., 2016), while complementing satellite measurements (Knox et al., 2017; Yan et al., 2019). For example, methodologies developed by Gu et al (2009) utilize carbon exchange data to assign 5 distinct periods to the vegetation growth cycle based on annual trajectories of plant community carbon dynamics, giving ecological relevance to phenological stages (i.e., phenoperiods). Placing spectral and ecosystem carbon exchange information into these phenoperiods provides critical information about changes in ecosystem carbon dynamics in context of seasonal ecological change (Trifunovic et al., 2020; Vázquez-Lule and Vargas, 2021).

Our overarching goal is to test the performance of proximal sensors to predict phenoperiod dates and track vegetation carbon phenology based on net ecosystem productivity (NEP) within a temperate salt marsh. Theoretically, NEP represents the net carbon balance integrated from all biochemical processes occurring across the ecosystem. We compare vegetation reflectance indices and spectral bands derived from commonly used proximal sensors (i.e., phenocam, SRS) and spaceborne platforms (i.e., MODIS). While vegetation reflectance patterns in temperate terrestrial ecosystems usually follows the annual course of net carbon exchange (Wu, 2012; Balzarolo et al., 2016), it is unclear if these expected relationships are consistent in ecosystems representing the terrestrial-aquatic interface (i.e., salt marshes).

We hypothesize that: (1) all sensors and indices will be able to track the annual course of NEP, yet proximal sensors are expected to have higher agreement with NEP than NASA's Moderate Resolution Imaging Spectroradiometer- (MODIS) derived indices. Proximal sensors offer higher temporal resolution, better representation of the local footprint of NEP and have reduced atmospheric interference. This should be especially relevant for phenocam images which, depending on specific configuration, offers larger viewing fields and integrates a larger canopy swath. In many cases MODIS-derived indices correlate relatively well with ground-based sensors (St Peter et al., 2018; Filippa et al., 2018), but for coastal environments there is higher uncertainty (Feagin et al., 2020; O'Connell et al., 2017; Vázquez-Lule et al., 2019). Further, the daily time acquisition of proximal sensors should be able to represent more pertinent information on marsh biogeochemistry (i.e., salinity and tide influences); (2) indices which incorporate an infrared band are expected to perform better than indices based solely on visible wavelengths as more information is relayed on physiological function in regard to canopy structure, water content, pigmentation and photosynthetic capacity (Badgley et al., 2017). Wavelengths not directly absorbed by photosynthetic tissues (i.e., near-infrared) can offer greater physiological detail while responding to changes in plant functional traits (Ollinger, 2011). We recognize that uncertainties remain for coastal wetlands where exposed sediments, surface water and elevated soil moisture may influence spectral reflectance. Generally, while healthy vegetation strongly reflects NIR while absorbing RED, soils reflect both NIR and RED wavelengths yet wet soils reflect considerably less in both bands due to strong absorption by water molecules (Ghulam et al., 2007; Foroughi et al., 2020). The current study is novel as it quantifies how different proximal sensors, MODIS, vegetation indices and spectral bands respond to the unique properties of salt-marsh vegetation and how well these reflectance properties align with changes affecting NEP in this understudied ecosystem.

2. Materials and methods

2.1. Study site

The study site is the St Jones Reserve (39.09 °N, 75.44 °W) which is part of the Delaware National Estuarine Research Reserve (DNERR) and the National Estuarine Research Reserve System (NERRS) supported by NOAA (Fig. 1). The site is designated as a native brackish tidal salt marsh, influenced hydrologically by both the St. Jones river (average salinity, 8.2 ± 1.8 ppt) and ocean waters from the Delaware Bay (Capooci et al., 2019). The climate is humid subtropical (Cfa) with an annual average air temperature and total annual precipitation of 13.8 °C and 1117 mm, respectively.

Vegetation is dominated by *Spartina alterniflora* L. (saltmarsh cordgrass; recently referred to as *Sporobolus alterniflorus*; Peterson et al., 2014) which displays strong seasonal growth cycles. There is approximately 11 km^2 of continuous marsh vegetation intermixed with meandering tidal channels associated with variable water levels, driven

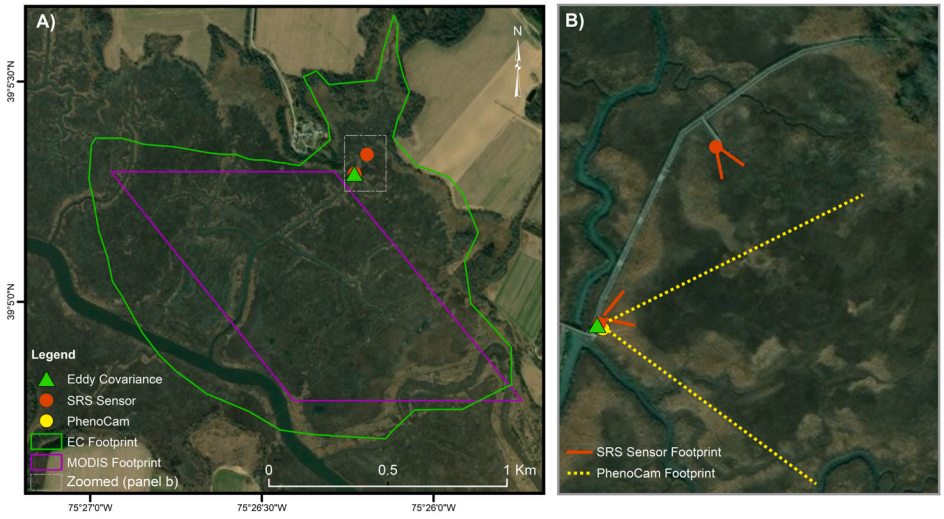

Fig. 1. Study site location showing A) eddy covariance (EC) flux tower filtered footprint (green) and Moderate Resolution Imaging Spectroradiometer (MODIS) footprint (purple); B) zoomed area showing EC tower location and proximal sensor viewing angles/footprint estimations. Service Layer Credits: Source: Esri, DigitalGlobe, GeoEye, Earthstar Geographics, CNES/Airbus DS, USDA, USGS, AeroGRID, IGN, and the GIS User Community. (For interpretation of the references to color in this figure legend, the reader is referred to the web version of this article.)

by subordinate tides. Finally, this marsh rarely gets flooded, which contrasts from low marshes that get flooded during every high tide. Thus, our spectral measurements mostly represent characteristics of vegetation as the canopy is never submerged. To further investigate any impacts of flooding on proximal sensor data, we flagged daily reflectance when the main tidal creek exceeded a threshold of 0.7 m above mean sea level during a midday window (11:00–13:00), when reflectance data was captured. Exceeding this threshold (0.7 m) results in standing water above marsh sediments, yet we did not observe any impacts which would significantly influence annual reflectance curves (Figs. S1 and S2). The site is part of both the AmeriFlux network (site ID: US-StJ) and phenocam networks (site ID: stjones).

2.2. Eddy covariance measurements

NEP was measured using the EC technique (Baldocchi, 2003; Aubinet et al., 2012) with an enclosed path infrared gas analyzer (Li-7200, Licor, Lincoln, NE, USA) and 3D sonic anemometer (Gill Windmaster Pro, Gill Instruments, Lymingtonm, UK) recording measurements at 10 Hz. A detailed description of the EC system and data processing is available elsewhere (Vázquez-Lule and Vargas, 2021). We selected a two-year period spanning 2017–2018 to ensure complete data for both flux and reflectance measurements. Briefly, preprocessing and flux corrections were performed using EddyPro software (version 7.0.6) and included time lag compensation, double coordinate rotation on wind components and Reynolds block averaging to arrive at 30 min flux intervals of NEP. Additional processing included removal of flagged instrument QA/QC values, removal of flux outliers falling beyond a range of -50 to 50 μmol CO_2 m^{-2} s^{-1}, footprint filtering to the confines of marsh vegetation (Fig. 1A) and removal of values associated with low turbulence which occurred mainly during nocturnal hours. This resulted in removal of 41% and 48% of fluxes for 2017 and 2018, respectively. We implemented the footprint model of Kljun et al. (2004) which functions similar to the Kormann and Meixner (2001) model that has previously been field validated in short canopy grasslands (Arriga et al., 2017). Gaps were filled with a marginal distribution sampling (MDS) moving look-up table utilizing meteorological variables collected on site as described in Vazquez-Lule and Vargas (2021).

2.3. Phenocam measurements

Canopy level images were taken using a "phenocam" (NetCam 1.3 megapixel SC IR security camera, StarDot Technologies, Buena Park, CA, USA). The phenocam is located on the upper most portion of the EC tower, 2.8 m above the canopy and is positioned eastward at an oblique orientation capturing a large swath of canopy (Fig. 1B). Since the camera acquires an image every 30 min from sunrise to sunset, we selected a single daily midday true color image (containing red, green and blue visible wavelengths; RGB) and a single midday near infrared image (NIR) taken several minutes apart (allowing time for removal of a mechanical infrared filter) to reduce effects from variable illumination. Exact time of day for midday image acquisition ranged from 12:00 to 12:15. This collection of daily images was inspected visually for any obvious distortions and filtered for occasional hazy or foggy images (hazer R package, Seyednasrollah, 2018), which removed 30 (8.2%) and 42 (11.5%) images for 2017 and 2018, respectively. Phenocam data was downloaded from the University of New Hampshire central phenocam server (https://phenocam.sr.unh.edu/webcam/) (Seyednasrollah et al., 2019).

A midsummer image was used to delineate a region of interest (ROI) to set a boundary on visible and infrared digital number (DN) extraction using a pixel averaging approach. We selected a spatially inclusive ROI which covers large areas of continuous marsh vegetation while encompassing the eastern portion of the EC footprint. Since a DN is not directly relatable to reflectance measurements we used the relative red (red chromatic coordinate; RCC) and back-calculated NIR from total scene brightness for single band comparisons. Next, we applied raw data filters in consecutive order consisting of a cubic smoothing spline followed by a max filter which selects values falling within the upper 90th percentile over a three-day moving window (Migliavacca et al., 2011; Sonnentag et al., 2012). Any short gaps created from removal of unacceptable images or filtering steps were filled via linear interpolation. Most images that were removed occurred during winter storm events, when the spectral response is constant, thus there was minimal impact on the trajectory of seasonal reflectance.

Since the phenocam image sensor operates differently than a traditional spectral reflectance sensor we have applied suggested scaling factors to each final phenocam indice or spectral band based on the corresponding MODIS index or band (Filippa et al., 2018; Petach et al., 2014). Scaling was completed year-wise using the same 3 × 3 MODIS pixel grid that we used for our spectral comparisons.

2.4. SRS measurements

Normalized difference vegetation index (NDVI) spectral reflectance sensors (SRS) (Meter Inc, Pullman, WA, USA) were positioned in 2 separate locations approximately 100 m apart with readings recorded every 5 min (Fig. 1B). Although proximal sensor footprints are largely determined by viewing angle and orientation, following common installation protocols, SRS sensors in our set-up have spatially limited

viewing footprints in comparison to the phenocam and EC tower (Fig. 1), thus using a mean value from multiple sensors provides a more comprehensive ecosystem-scale assessment. Since there is greater noise associated with high frequency SRS data due to changes in solar position and illumination, we selected readings from a two-hour midday window (11:00–13:00) which was used to generate daily averages. We then applied data filters described above and filled any short gaps with linear interpolation. For RED reflectance we applied a Savitzky–Golay filter to reduce noise in the data.

2.5. Moderate resolution imaging spectroradiometer

NDVI and enhanced vegetation index (EVI), NIR and RED band data from MODIS (MOD13Q1 16 day, 250 m vegetation indices product) was downloaded from Oak Ridge National Lab distributed active archive center (ORNL DAAC) global subset tool (https://modis.ornl.gov/globalsubset/) for an area of 750 km^2 (9 pixels) which encompassed most of the EC tower flux footprint while excluding pixels from surrounding land cover (Fig. 1A). The MOD13Q1 product pre-processing includes atmospheric correction from bi-directional surface reflectance and masking from water, clouds and aerosols. For RED reflectance we again applied a Savitzky–Golay filter to reduce noise in the data.

2.6. Meteorological measurements

A meteorological station located on site near the EC tower collected information on air temperature and humidity (HC2-S3, Campbell Scientific, Logan, UT) precipitation (TE 525, Tipping Bucket Rain Gauge, Campbell Scientific, Logan, UT), and photosynthetically active radiation (PAR) (SQ-110, quantum sensor, Apogee, Logan, UT). Air temperature, humidity and PAR were measured every 5 s and averaged at 30-min intervals. Precipitation was calculated as a daily total. Vapor pressure deficit (VPD) was calculated using air temperature and relative humidity based on Tetens formula (Murray, 1967). For calculation of daily PAR only daytime readings were considered (PAR > 20 μmol m^{-2} s^{-1}).

2.7. Vegetation indices

Indices incorporating solely visible wavelengths derived from phenocam included the vegetation contrast index (VCI; Eq. (1)) (Zhang et al., 2018) and widely used green chromatic coordinate (GCC; Eq. (2)) (Sonnentag et al., 2012). For all listed vegetation indices, general spectral band names are listed, for specific bandwidths see Table 1.

$$VCI = \frac{GREEN}{(RED + BLUE)} \tag{1}$$

$$GCC = \frac{GREEN}{(RED + GREEN + BLUE)} \tag{2}$$

Phenocam NDVI and EVI were calculated using standardized protocols in phenopix Eqs. (3) and ((4)) (Filippa et al., 2018; Petach et al., 2014). Since the phenocam is not a traditional reflectance sensor, we list estimated spectral wavelengths based on previous comparisons with a spectroradiometer (Table 1) (Petach et al., 2014). Phenocam EVI constants adapted in phenopix were the same as implemented by MODIS (MOD13Q1), i.e., as a modification of NDVI (Liu and Huete, 1995) ($G = 2.5$, $C1 = 6$, $C2 = 7.5$, $L = 1$). We also used RCC as a proxy for RED, the NIR signal and the combined product of NIR and NDVI as another newly developed index which isolates NIR reflectance derived solely from vegetation (Camera NIRv; Badgley et al., 2017). In the special case of RED reflectance, since RED is strongly absorbed by healthy vegetation, we needed to invert annual curves to enable proper fitting based on the change in decreased reflectance. This resulted in some values being negative, so we simply set the minimum value of the inverted curve to zero.

Table 1
Spectral bandwidth ranges for phenocam*, SRS sensors and MODIS.

EM value	Phenocam (nm)	SRS (nm)	MODIS (nm)
Blue	430–515	–	459–479
Green	510–570	–	545–565
Red	575–710	645–655	620–670
NIR	800–815	805–815	841–876

* Bandwidths listed for phenocam were estimated from spectroradiometer comparisons (Petach et al., 2014).

$$NDVI = \frac{(NIR - RED)}{(NIR + RED)} \tag{3}$$

$$EVI = G \times \frac{(NIR - RED)}{(NIR + C1 \times RED - C2 \times BLUE + L)} \tag{4}$$

For the SRS sensors, we used NDVI as calculated by the instrument (Eq. (3)), EVI2 (Eq. (5)) the standalone RED and NIR signals and the combined product of NDVI and NIR to generate SRS NIRv (Gamon et al., 2015). Since blue is not available for the SRS sensor, we substituted EVI2 as a comparable alternative (Eq. (5); Jiang et al., 2008). For clarity, we will simply refer to EVI2 as EVI in the subsequent text since we are using it as a proxy exclusively for SRS sensors. For MODIS we used the prepared 16-day vegetation indices product of NDVI and EVI, the standalone RED and NIR signals and the combined product of NDVI and NIR to generate NIRv. We used the same adjustment method for RED reflectance for both SRS sensors and MODIS bands by inverting the annual reflectance curve and setting minimum values to zero.

$$EVI\ 2\ (EVI\ proxy) = G \times \frac{(NIR - RED)}{NIR + (2.4 \times RED) + L} \tag{5}$$

2.8. Phenological metrics and data analysis

We used the phenopix R package for processing daily phenology time series of EC, phenocam, SRS and MODIS data (Phenopix R package; Filippa et al., 2016). As we aim to make comparisons across several phenological datasets we used as much of the same processing steps as possible including filtering of raw data, gap filling, curve-fit functions and phenoperiod breakpoint algorithms. Annual trajectories were fit with a double logistic function and phenoperiod breakpoint detection method specifically developed for carbon phenology applications (Gu et al., 2009). Uncertainty was estimated by bootstrapping curve fits 500 times based on random noise in daily data to create an ensemble of curves, we report median values and a confidence interval indicating the 10th and 90th percentiles of the distribution of generated phenoperiod transition dates (Filippa et al., 2016).

NEP derived from EC measurements was used as a benchmark for defining phenoperiod transitions based on site carbon phenology. We used this benchmark to compare indices and spectral bands generated from phenocam and reflectance sensors. Following conventions established by Gu et al. (2009), there are 5 distinct phases of seasonal vegetation productivity (i.e., pre, recovery, stable, senescence and termination phases) marked by ecologically meaningful transitional phase changes. These periods consist of upturn day (UD), stabilization day (SD), downturn day (DD) and recession day (RD), which are similar to traditional phenological change terminologies (e.g., green-up, maturity, senescence and dormancy) (Filippa et al., 2016; Gu et al., 2009). After entering the spring recovery phase, rates of carbon sequestration quickly increase reaching a steady state maximum at the stabilization day. Maximum rates are maintained over the stable period before initiation of a rate decrease on the downturn day. As rates of net productivity continue to decrease, the system transitions back to a net carbon source marking the recession day and onset of the dormancy period. Additional information was calculated including overall length

of the carbon sink season, as the timing between recession and upturn days (Gu et al., 2009) and maximum increasing (recovery/green-up) and decreasing (senescence) rates of spring and fall transitional change (Filippa et al., 2016).

To gain insight on which sensors and VI's are best able to track daily changes in carbon phenology, ordinary least squares (OLS) linear models were assembled for each NEP-VI relationship. Models were assembled using combined data from both study years and assessed using 5-fold cross validation with R^2 and root mean square error (RMSE) metrics. We also completed simple regression models individually for each year to assess the degree of interannual variation in the NEP-VI relationships. In addition, proximal sensor indices and spectral bands were compared to corresponding MODIS indices and bands. All data preparation, preprocessing and analysis was completed using R open-source software version 3.6.1 (R Core Team 2019).

3. Results

3.1. Net ecosystem productivity benchmarks and climate

Daily mean NEP was statistically similar between years (p=0.567, t-test using daily data) with overall means of 0.53 ± 1.58 and 0.45 ± 2.00 μmol CO_2 m^{-2} s^{-1}, for 2017 and 2018 (± sd). Daily daytime mean NEP, the benchmark to define site carbon phenology, was also statistically similar (p=0.797) with overall means of 2.85 ± 4.15 and 2.93 ± 4.84 μmol CO_2 m^{-2} s^{-1} for 2017 and 2018 (Fig. 2). The annual sum of NEP was 199.2 ± 5.7 and 170.3 ± 5.9 g C m^{-2} yr^{-1} for 2017 and 2018.

On a monthly basis, daily rates were also statistically similar, especially during summer and fall months, with only December, January and March showing significant differences (p<0.01). In 2018, the upturn day, which marks start of carbon sink season (i.e., NEP > 0), was reached 10 days later while stabilization was reached earlier (DOY 150, 2018 vs. DOY 159, 2017), resulting in a shorter recovery period (46 days vs. 27 days for 2017 and 2018). Despite differences in early season phenology the stable period was similar between years (77 days vs. 80 days for 2017 and 2018), yet 2018 had higher peak values and downturn day arrived 6 days later and persisted longer with dormancy onset 10 days later, extending the senescence period (72 days vs. 88 days for 2017 and 2018). The curve shapes of daytime NEP were different, yet in both years there was faster recovery rates in spring and slowed rates of senescence in fall (Fig. 2).

Meteorological data showed differences between years (Fig. 3, Table S1), especially during late winter and spring of 2018 where greater winter chill was followed by suppressed springtime temperatures. The cumulative late winter-early spring (months of JFMA) temperature was 11.2 °C cooler during 2018 compared to 2017. Mean annual precipitation totals were comparable between years (28 mm and 34 mm for 2017 and 2018) yet when considering monthly totals, similarities rarely coincided between years. Differences were greatest during fall and winter months of 2018 when the site received twice as much precipitation compared to the same period in 2017.

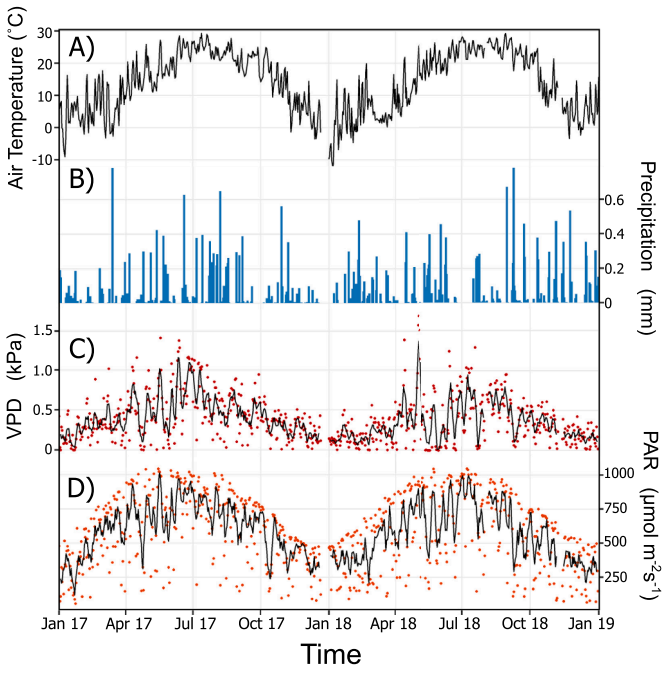

Fig. 3. Daily mean meteorological data for: A) air temperature (black), B) precipitation (blue), C) vapor pressure deficit (red) with 5 day rolling mean (black), D) daytime photosynthetically active radiation (PAR) (orange) with 5 day rolling mean (black). (For interpretation of the references to color in this figure legend, the reader is referred to the web version of this article.)

3.2. Phenoperiods and transition dates

Comparing phenoperiod dates generated from proximal sensors and MODIS with carbon phenology dates derived from site NEP (Fig. 4), the prediction of upturn day was best captured by VCI and GCC (1–3 days ahead of benchmark, 2017 and 3–4 days behind benchmark, 2018) and NDVI (7 days ahead, 2017 and 5 days behind, 2018) from the phenocam and NIRv from SRS sensors (1 day ahead, 2017 and 2 days behind, 2018). Other NIR containing phenocam indices were variable (EVI, NIRv), yet of these, NIRv had the best interannual consistency (5–12 days ahead). SRS NDVI consistently underpredicted the upturn day (5-21 days behind) while EVI offered some improvements (1–13 days behind). Primary indices from MODIS consistently underpredicted this key transition date with the most discrepancy, approximately 6–30 days prior to actual onset of the carbon sink season. While NIR reflectance was more variable, RED tended to underpredict for proximal sensors

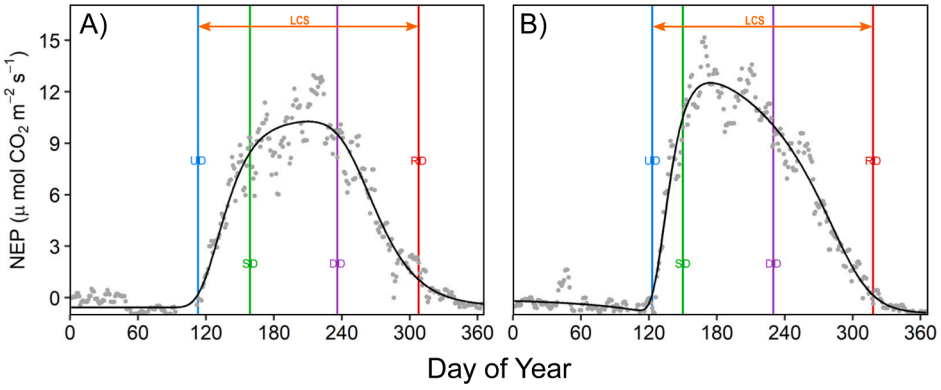

Fig. 2. Annual trajectories of daily daytime mean NEP for A) 2017 and B) 2018 with key phenology metrics of upturn day (UD) (blue), stabilization day (SD) (green), downturn day (DD) (purple), recession day (RD) (red) and length of carbon sink (LCS) (orange). Grey points represent filtered daily daytime NEP and solid black line is the median value of 500 curve fit ensembles. (For interpretation of the references to color in this figure legend, the reader is referred to the web version of this article.)

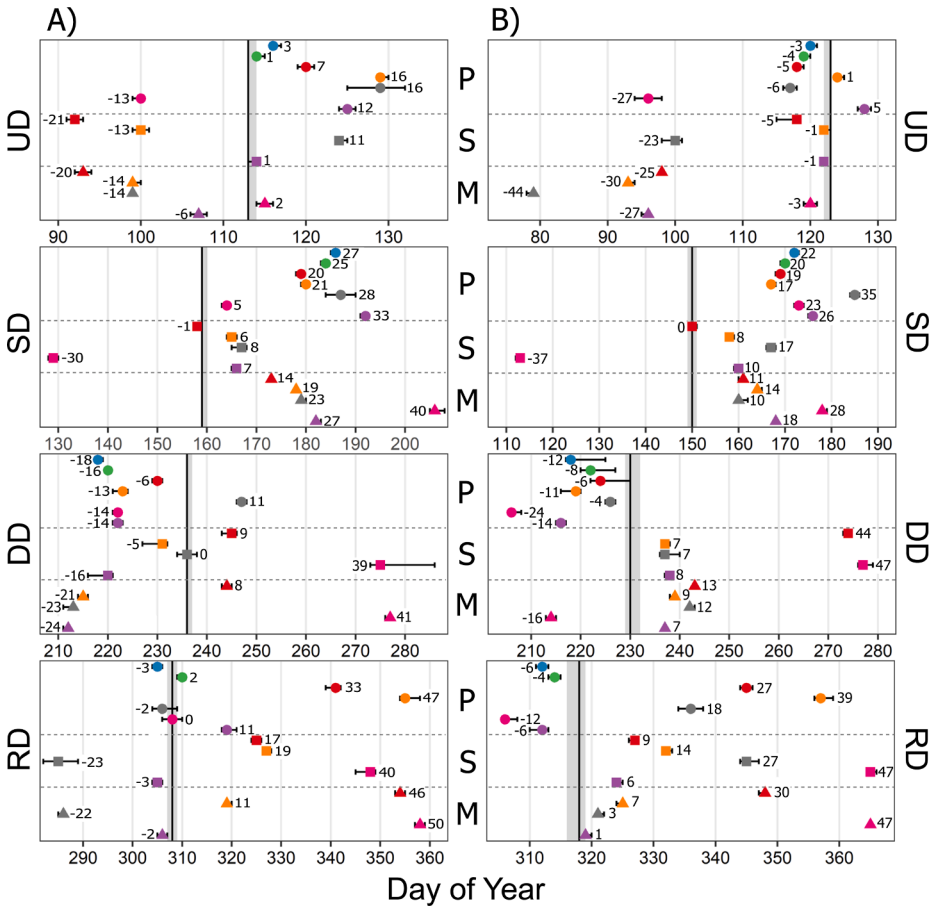

Fig. 4. Phenoperiod transition date comparisons for A) 2017 and B) 2018 between phenocam (P) (circle), SRS sensors (S) (square), MODIS (M) (triangle) and NEP benchmarks (vertical black lines). Numbers indicate days deviation from the median value of NEP benchmarks. UD (upturn day), SD (stabilization day), DD (downturn day) and RD (recession day). VCI (blue), GCC (green), NDVI (red), EVI (orange), NIR (grey), RED (pink) and NIRv (purple). Error bars and width of vertical grey bars represent the 10th and 90th percentiles from curve fit bootstrapping. (For interpretation of the references to color in this figure legend, the reader is referred to the web version of this article.)

(13–27 days behind for phenocam, 100–121 days behind for SRS).

Phenocam indices consistently overpredicted onset of stabilization (17–33 days ahead) while SRS indices generally performed better (1 day behind to 10 days ahead). MODIS indices also overpredicted stable period onset (11–27 days ahead). NDVI and EVI were the best preforming indices for all sensors, predicting within 17–21 days for phenocam, 1–10 days for SRS and 11–19 days for MODIS. There was a tendency for NIR to overpredict across sensors yet RED was more variable with smaller overpredictions from phenocam (5–23 days ahead), yet large underpredictions from SRS (30–37 days behind) and MODIS (28–40 days ahead).

The downturn of maximum net productivity from tower NEP showed only a 6-day interannual difference and primary phenocam indices predicted within a similar annual window (DOY 220–230), with these dates always occurring prior to the rate decrease in net productivity (6–18 days behind, 2017 and 6–14 days behind, 2018). SRS sensors were more variable as was MODIS, especially for EVI and NIRv where there was inconstancy in date directionality (underpredictions in 2017, overpredictions in 2018) while NDVI consistently overpredicted (9–44 days ahead for SRS and 8–13 days ahead for MODIS). NIR across sensors generated a date range similar to other indices and this was also true of RED for phenocam, but for SRS and MODIS RED tended to overpredict.

The prediction of the recession day was best captured by MODIS NIRv (2 days behind to 1 day ahead). Followed by phenocam visible wavelength indices (6 days behind to 2 days ahead), SRS NIRv (3 days behind to 6 days ahead), and phenocam NIRv (11 days behind to 6 days ahead). Other indices which incorporate NIR wavelengths overestimated season end dates, with phenocam NDVI and EVI ahead 37–47 days, SRS NDVI and EVI ahead 9–19 days and MODIS NDVI and EVI ahead 7–46 days. As with the upturn day, NIR was variable across sensors tending towards underprediction in 2017 and overprediction in 2018, yet RED generated considerable overpredictions for both SRS (40–47 days ahead) and MODIS (47–50 days ahead).

3.3. Length of carbon sink season and transitional rates of phenological change

Although season start and end dates were different between years, overall length of the carbon sink period was identical (195 days). Since LCS is defined by upturn and recession days, sensors and indices which best predict these dates in relation to tower NEP will have the best LCS estimates, but this is also the case for indices which have consistent offsets between season start and end dates (i.e., predict right for the wrong reason). The best and most consistent LCS season estimates due to correct UD and RD prediction were generated from phenocam visible wavelength indices which fell within 1–6 days for 2017 and 0–3 days for 2018 (Fig. 5).

This was closely followed by NIRv from SRS sensors and MODIS (more variable) which fell 4–7 and 4–28 days ahead of the actual carbon sink length, respectively. However, NIRv from phenocam differed by overpredicting season start dates and good agreement in 2017 (within 1 day) was due to consistent overprediction offsets which did not occur for 2018 where RD was underpredicted (within 11 days). Other primary indices considerably overpredicted LCS season with estimates ranging from 14 to 66 days ahead of tower NEP benchmarks. Largest overpredictions in this category were from MODIS NDVI (66 and 55 days ahead for 2017 and 2018). Similar to phenoperiod date predictions, NIR caused variable LCS estimates (underpredictions in 2017 and overpredictions in 2018) while SRS and MODIS RED caused the largest overpredictions (48–168 days ahead).

We also examined sensors and indices for ability to capture maximum rate increases at which the system becomes a net carbon sink

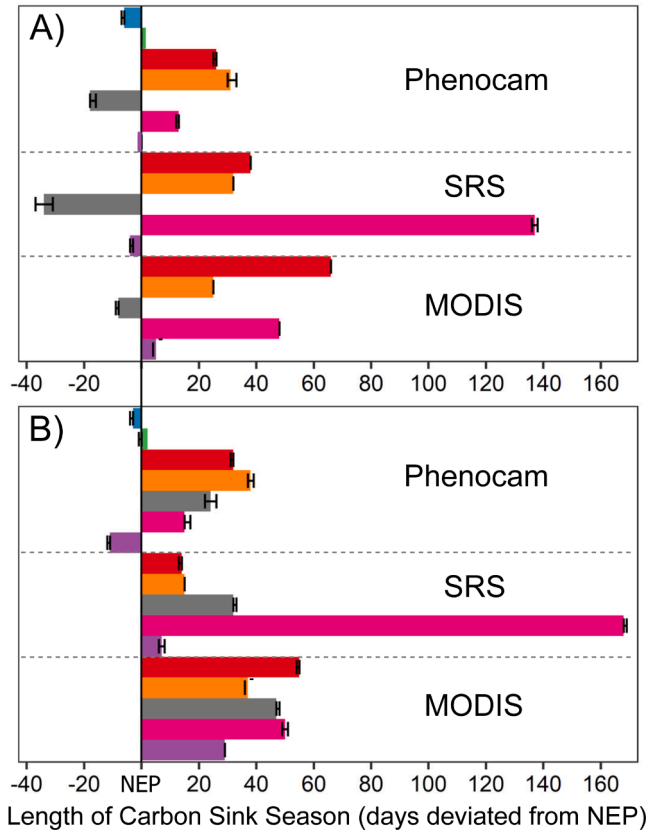

Fig. 5. Length of carbon sink season for A) 2017 and B) 2018. Solid vertical black line is length of net carbon sink season determined from NEP (195 days for both 2017 and 2018). VCI (blue), GCC (green), NDVI (red), EVI (orange), NIR (grey), RED (pink) and NIRv (purple). Error bars represent the 10th and 90th percentiles from curve fit bootstrapping. (For interpretation of the references to color in this figure legend, the reader is referred to the web version of this article.)

during recovery and conversely, the maximum rate of decreasing net carbon sink during senescence (Fig. 6). Reported rates are unitless as we scaled and standardized all indices for ease of comparison across sensors with different output ranges. Rates of increasing carbon sink observed from tower NEP occurred nearly 2 times faster during 2018 (0.096) compared to 2017 (0.054) yet rates of decrease were similar (-0.035 and -0.027 for 2017 and 2018). There was relatively tight grouping, indicating that all sensors and indices were able to capture similar rates of spring and fall phenological change. Rates of increase in spring tended to be underestimated by sensors and indices but the magnitude of separation was greater during 2018. Indices from the SRS sensor (NDVI, EVI, NIRv) tended to capture rates of increase most similar to NEP. Rates of decrease were more variable between years with most indices decreasing slower than tower NEP in 2017 and faster in 2018.

3.4. Tracking net ecosystem productivity

All vegetation indices were able to track annual changes in NEP, yet curve architecture and magnitudes did not always coincide with the course of NEP (Fig. 7).

The greatest signal noise was generated by NIR and RED wavelengths from phenocam and SRS sensors. The least noise was generated from phenocam GCC and NIRv, and SRS NDVI and NIRv, the latter coincides with reduced spectral bandwidths (i.e., larger bandwidths create more signal noise). During dormancy periods we expect that curves should become constant from reduced spectral response, yet there was some degree of signal carry over into dormancy for primary indices which utilize RED and NIR bands, although this was not as obvious for SRS sensors.

Results from combined year ordinary least squares (OLS) regression modeling shows that nearly all sensors and associated primary vegetation indices strongly correlate with site NEP (R^2 = 0.81-0.93) (Fig. 8, Table 2). Best fits were from phenocam visible wavelength indices (R^2 = 0.92–0.93) while the next best clustering consisted of phenocam NDVI (R^2 = 0.89), SRS EVI (R^2 = 0.89), MODIS NDVI and EVI (R^2 = 0.87 to 0.90) and SRS and MODIS NIRv (R^2 = 0.88). This was followed by phenocam EVI and NIRv (R^2 = 0.81–0.83) and SRS NDVI (R^2 = 0.84). Fits with least agreement were produced by NIR (R^2 = 0.69–0.81) and RED bands (R^2 = 0.37–0.73) although NIR still had arguably strong correlations with NEP.

In fall, NEP values were typically lower at a specified VI value than the corresponding VI value in spring where NEP was higher. This separation in spring-fall NEP-VI values was most apparent for phenocam indices, especially NDVI and EVI, yet most sensors and indices displayed some degree of disparity between spring and fall values. Looking at individual year regressions, this was consistent between years (see year-wise models, Figs. S3 and S4). The pattern was less obvious with 16-day MODIS data.

We also compared indices from proximal sensors with corresponding MODIS indices (Fig. 9), to gain insight on how reflectance is related at different spatial domains and to inspect relationships between proximal sensors and MODIS. The comparison of RED and NIR components was very similar between proximal sensors and MODIS with moderately strong relationships with NIR and a much weaker relation with RED. Primary indices had strong agreement with phenocam NDVI yet there were clear differences between proximal sensors with phenocam NDVI and SRS EVI and NIRv preforming best.

4. Discussion

This study tests common proximal sensors and MODIS-derived indices to predict phenoperiod transition dates and monitor ecosystem carbon phenology within a salt marsh. We postulated all sensors and indices have the ability to track changes in NEP, but proximal sensors should perform better by offering higher temporal resolution and greater footprint representation of the ecosystem, while minimizing atmospheric interference or issues with mixed pixels. Our hypothesis was supported for tracking and generally supported for phenoperiod date predictions. As postulated, phenocam tracking and phenology metrics closely aligned with tower NEP as the vegetation footprint is larger and more inclusive compared to spatially limited SRS measurements. We expected indices which incorporate infrared wavelengths to perform better as information is relayed on factors which affect plant physiological function and metabolism, yet this was not the case. Our results highlight that salt-marsh vegetation poses several challenges when dealing with commonly applied vegetation indices (NDVI, EVI), especially for season start and end dates. These findings provide insights to improve our understanding of carbon phenology and vegetation reflectance dynamics in underrepresented salt-marsh ecosystems while providing sensor and vegetation-indices recommendations with comparisons across spatial scales.

4.1. Net productivity carbon phenology and interannual variation

Carbon phenology metrics defined by NEP integrates multiple ecological processes occurring across the landscape (Fatichi et al., 2019). We highlight that challenges exist in partitioning NEP into GPP and respiration within salt-marsh ecosystems as tidal flow, salinity and lateral transport of carbon can influence land-atmosphere mass exchange dynamics (Knox et al., 2018; Huang et al., 2019; Moffett et al., 2010, Trifunovic et al., 2020), and alter Q10 relationships (Wei et al., 2020). In this study, we focused on NEP measurements which provide a direct assessment of carbon phenology in an ecosystem with unique

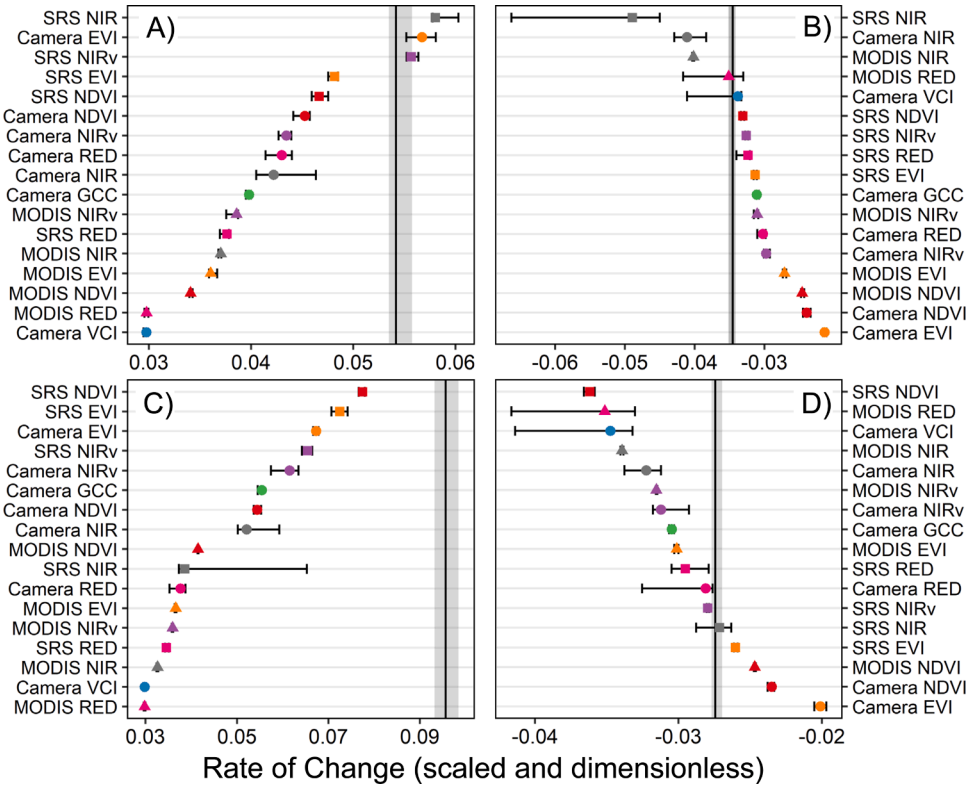

Fig. 6. Normalized rates of phenological change for A) recovery phase 2017, B) senescence phase 2017, C) recovery phase 2018, D) senescence phase 2018. Vertical black lines represent rates of change in NEP. VCI (blue), GCC (green), NDVI (red), EVI (orange), NIR (grey), RED (pink) and NIRv (purple). Circle (phenocam), square (SRS) and triangle (MODIS). Error bars and width of vertical grey bars represent the 10th and 90th percentiles of curve slopes from curve fit bootstrapping. (For interpretation of the references to color in this figure legend, the reader is referred to the web version of this article.)

biophysical controls without inserting confounded or biased information from a modelling approach for partitioning NEP. Our methodology is supported by several studies that have used measurements of net carbon exchange to track annual changes in carbon phenology (Garrity et al., 2011; Balzarolo et al., 2016; Zhao et al., 2020; Dronova et al., 2021). This method is also useful for applications aimed at reducing greenhouse gas emissions and monitoring to support carbon market and trading programs (Baldocchi et al., 2020) or assessing vegetation dynamics following marsh restorations (Negandhi et al., 2019; Tang et al., 2018).

Timing and duration of recovery and senescence periods varied between years, yet season length and interannual NEP totals were similar. This indicates that duration of carbon sink season as determined by UD and RD dates exerts more influence on annual budgets than approximate length of phenological periods, albeit transition dates of midseason metrics and rates of phenological change do exert influence in determining UD and RD dates (Gu et al., 2009). The onset of the 2018 recovery period was delayed 10 days compared with 2017 which likely stemmed from heighted winter chill that carried over to substantially reduce springtime temperatures. Severity of winter chill has been identified as a primary driver affecting greening onset in salt marshes and the date of this key transition exerts the most influence on subsequent photoperiods and overall growing season length (O'Connell et al., 2020). This may also explain why the recovery phase ended sooner, greatly reducing the length of the greening period (27 days in 2018 vs. 46 days in 2017). While the stable period was similar in length, the senescence period in 2018 spanned 16 days longer and extended 10 days later into the year. The exact mechanisms for these differences are beyond the scope of this paper, yet in 2018 during late fall early winter (OND months) we observed both greater precipitation (4.5 mm, 2018 vs. 1.9 mm, 2017) and lower tidal stream salinity (5.0 ppt, 2018 vs. 11.1 ppt, 2017). Previous studies have reported that changes in salinity are associated with fluctuations in greenhouse gas emissions in this salt marsh (Capooci et al., 2019; Seyfferth et al., 2020). Furthermore, we postulate these events played a role extending the senescence period as precipitation can influence temporal variations in greenness (Zhu et al., 2019) and salinity levels over 12 ppt have been shown to decrease rates of productivity in *S. alterniflora* (Courtney et al., 2016). Climate factors play an important role in determining length and transitional dates of phenoperiods, yet within the salt marsh there appears some degree of resiliency to interannual weather patterns as there was only a 28.9 umol m^{-2} yr^{-1} difference between annual NEP totals.

4.2. Phenocam carbon phenology transition dates

Indices from the same sensor with spectral similarities had consistent phenoperiod prediction trends such as phenocam VCI and GCC visible wavelength indices or NDVI and EVI. Sometimes this was true across sensors such as NDVI from SRS and MODIS, but this was not always the case as different sensors utilize unique bandwidths and have different center points of electromagnetic reflectance (Table 1) (Huang et al., 2019; Dian et al., 2016).

Phenocam visible wavelength indices consistently performed best at detecting key season start and end dates. Other phenocam indices had larger discrepancies and consistently overestimated dormancy onset. This indicates a disconnection between both RED and NIR reflectance and fluxes which we attribute in-part to above-ground aerenchyma that directly bridges the soil-atmosphere interface, providing an abiotic mechanism which exerts influence on ecosystem scale fluxes. In some species such as *S. alterniflora*, ambient air is pulled through petioles and culms via pressure driven through-flow, thus increasing intercellular air spaces in aboveground tissues (Colmer and Flowers, 2008; Sorrell and Brix, 2013). This air space and resulting ratios of exposed mesophyll cells can strongly influence NIR reflectance (Slaton et al., 2001, Woolley, 1971). Based on evidence of plant mediated transport of methane in *S. alterniflora* (Tong et al., 2012), and seasonal peaks observed during fall months (Cao et al., 2020), a maximization of aerenchyma likely occurs later in the season which coincides with a period of maximal reflectance interference in NIR containing indices. Development of aerenchyma tissue exhibits a strong degree of plasticity in response to

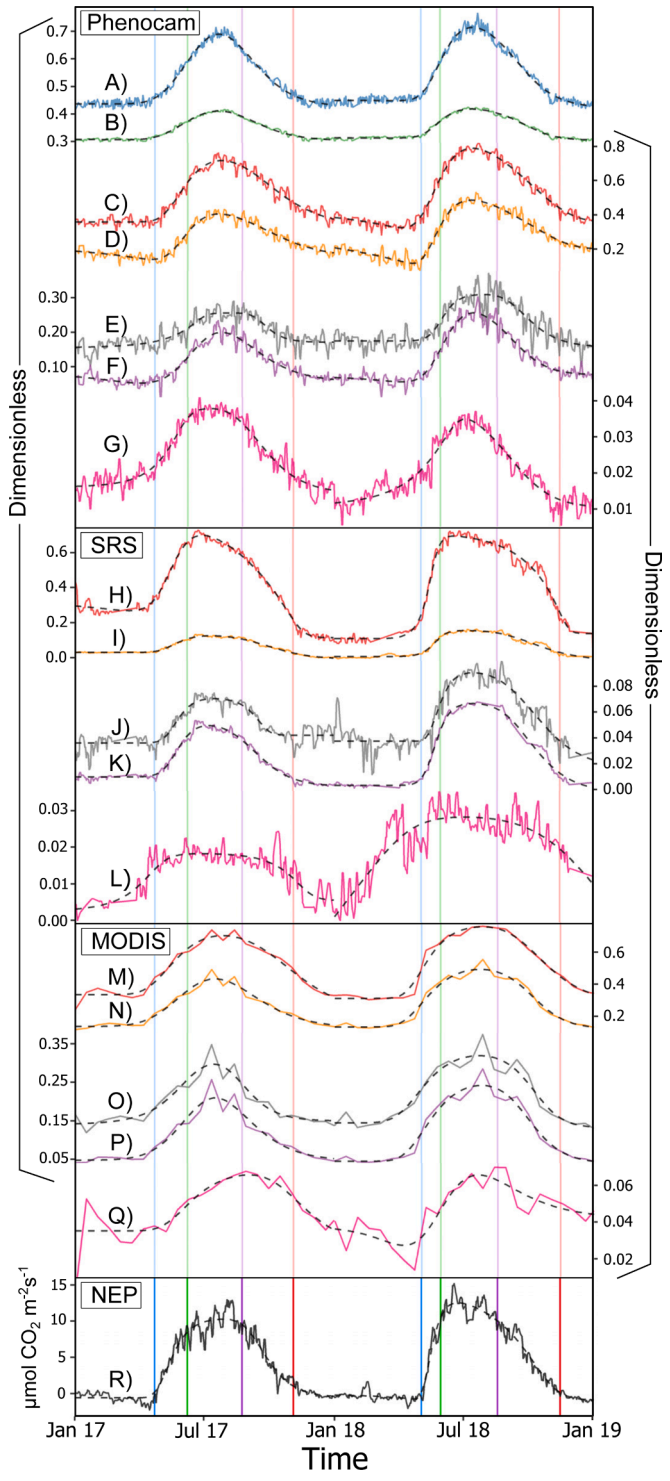

Fig. 7. Annual trajectories of daily vegetation indices and NEP. Phenocam: A) vegetation contract index (VCI), B) green chromatic coordinate (GCC), C) normalized difference vegetation index (NDVI), D) enhanced vegetation index (EVI), E) near-infrared (NIR), F) near-infrared of vegetation (NIRv), G) red chromatic coordinate (RCC). SRS: H) NDVI, I) EVI, J) NIR, K) NIRv, L) RED. MODIS (16-day): M) NDVI, N) EVI, O) NIR, P) NIRv, Q) RED. NEP: R) mean daytime NEP. Dashed lines represent best fit curves generated in phenopix. Vertical colored lines are NEP phenoperiod benchmark dates of upturn day (blue), stabilization day (green), downturn day (purple) and recession day (red). (For interpretation of the references to color in this figure legend, the reader is referred to the web version of this article.)

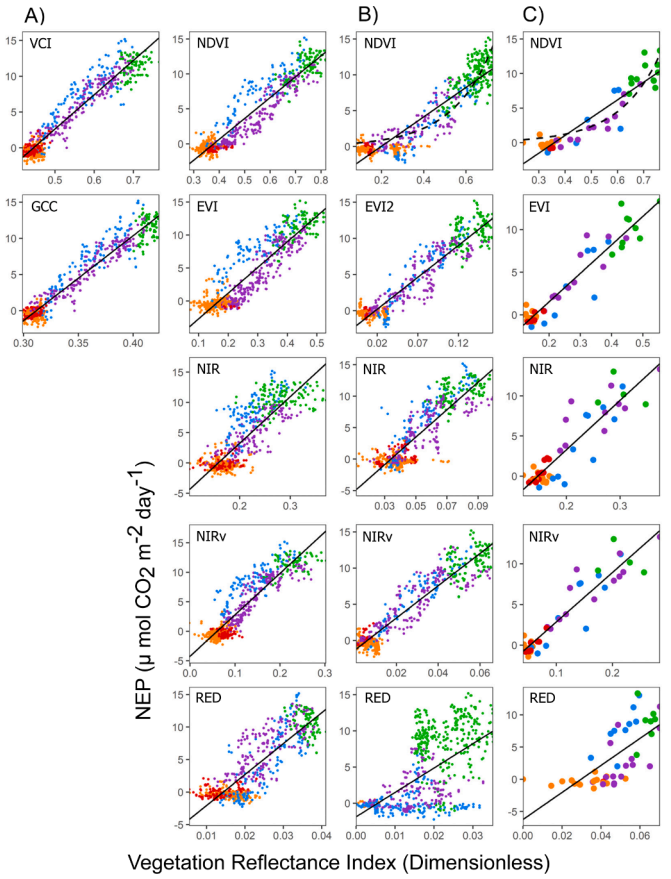

Fig. 8. NEP-VI relationships using daily data from A) phenocam, B) SRS and C) MODIS 16-day MOD13Q1 for combined years (2017–2018). Color coding represents phenoperiods as determined by sensor and vegetation index specific breakpoint results, blue = recovery period (green-up), green = stable period (maturity), purple = senescence period (senescence) and red/orange = dormant period/pre-season dormant period (dormancy). Solid black lines are linear fit and dashed lines are exponential fit, only shown for SRS NDVI ($R^2 = 0.89$) and MODIS NDVI ($R^2 = 0.90$). All models were significant ($p<0.001$). (For interpretation of the references to color in this figure legend, the reader is referred to the web version of this article.)

flooding and hypoxic soil conditions (Maricle and Lee, 2002). In much of the same way that soil temperature variations cause spatial variations in phenology (O'Connell et al., 2020), we postulate that site specific elevation gradients and hydrology may also play a role in heterogeneity of altered end of season reflectance signals via an uneven distribution of above ground aerenchyma across the landscape.

High percentages of standing dead biomass and exposed sediments containing organic matter also contribute to end of season discrepancies and these effects transfer over into the recovery period. It has been established that dead biomass and exposed soils can cause discrepancies in reflectance indices (Taddeo et al., 2019; Xu et al., 2014), while decoupling NEP-VI relationships (Rocha et al., 2008), and efforts at disentangling this interference has proved difficult (Ren and Zhou, 2019). Results from Knox et al. (2017) support our findings on the superior performance of visible wavelength indices in marsh environments where phenocam GCC performed better than NDVI in parametrizing a light use efficiency model to estimate productivity which was attributed to dead biomass. Similar effects have been confirmed from grasslands and deciduous forests where the trajectory of daily NDVI lags behind GCC as the latter is responsive to color changes and NDVI is sensitive to changes in leaf area (Filippa et al., 2018). Further, salt marsh sediments have persistently elevated soil moisture which can influence reflectance measurements when exposed. During spring (especially) and fall, when

Table 2
Combined year OLS linear model output summaries for phenocam, SRS sensors and MODIS using daily data. Note: all fits were significant ($p<0.001$).

Sensor	VI	Variables	Estimate	SE	*t*-value	RMSE	R^2
Phenocam	VCI	Intercept	−21.36	0.29	−74.58	1.40	0.92
		Slope	47.98	0.54	89.13		
	GCC	Intercept	−36.59	0.42	−87.93	1.25	0.93
		Slope	117.40	1.20	97.57		
	NDVI	Intercept	−11.29	0.20	−56.05	1.49	0.89
		Slope	29.86	0.38	77.99		
	EVI	Intercept	−6.57	0.20	32.83	2.12	0.81
		Slope	38.91	0.70	55.92		
	NIR	Intercept	−12.12	0.40	−30.12	2.78	0.69
		Slope	76.94	1.89	40.67		
	NIRv	Intercept	−4.22	0.15	−28.01	1.80	0.83
		Slope	70.23	1.16	60.40		
	RED	Intercept	−6.82	0.26	−26.72	2.46	0.73
		Slope	476.27	10.72	44.43		
SRS	NDVI	Intercept	−4.04	0.14	−28.62	1.97	0.85
		Slope	20.50	0.32	63.37		
	EVI	Intercept	−1.55	0.09	−17.21	1.57	0.89
		Slope	88.24	1.14	77.58		
	NIR	Intercept	−7.38	0.24	−30.28	2.33	0.76
		Slope	217.81	4.46	48.81		
	NIRv	Intercept	−1.31	0.09	−14.15	1.72	0.88
		Slope	211.91	2.89	73.40		
	RED	Intercept	−1.87	0.30	−6.109	4.00	0.37
		Slope	336.64	16.24	20.73		
	NDVI	Intercept	−9.22	0.75	−12.22	1.14	0.87
		Slope	25.70	1.45	17.73		
	EVI	Intercept	−5.15	0.47	−10.90	0.80	0.90
		Slope	33.39	1.63	20.39		
	NIR	Intercept	−9.05	0.93	−9.705	1.37	0.81
MODIS		Slope	61.71	4.37	14.122		
	NIRv	Intercept	−3.20	0.42	−7.609	0.79	0.88
		Slope	60.73	3.23	18.811		
	RED	Intercept	−6.24	1.56	−3.998	3.39	0.47
		Slope	209.98	32.09	6.544		

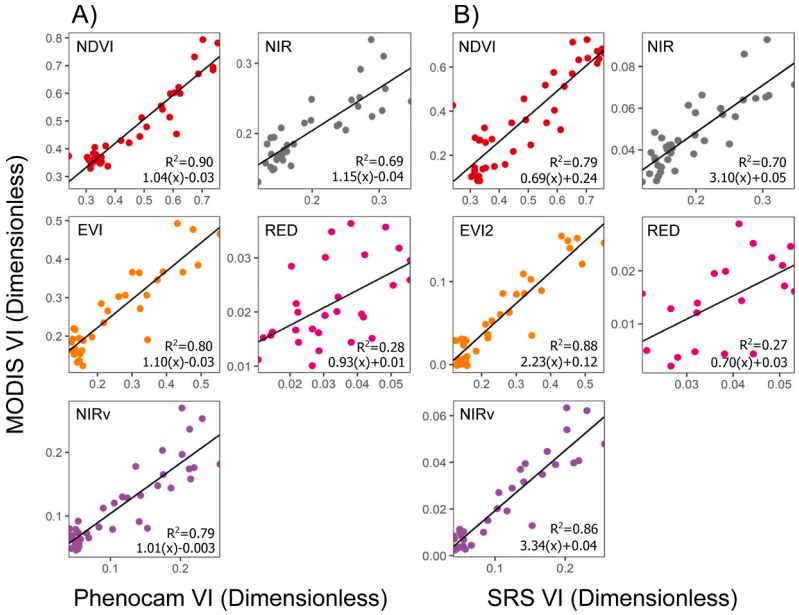

Fig. 9. Proximal sensor comparison with 16 day MODIS data. Color coding represents vegetation indices and reflectance bands, red = NDVI, orange = EVI, purple = EVI2, grey = NIR and pink = RED. Solid black lines are linear fit. All models were significant ($p<0.001$), RED models ($p<0.01$). (For interpretation of the references to color in this figure legend, the reader is referred to the web version of this article.)

vegetation is inactive, yet sediments are thawed, there is likely larger mismatch in reflectance/absorbance expectations as antecedent moisture strongly absorbs both RED and NIR wavelengths. While visible wavelengths indices (VCI, GCC) provide a measure of canopy greenness, this may not be consistently related with leaf chlorophyll concentration at higher midseason LAI's (Keenan et al., 2014), however it is plausible that shorter canopies which exhibit lower leaf area while lacking woody stems have higher coupling of greenness-pigment relationships. Thus, greenness may infer functionality better within the salt marsh while also providing an estimate of the annual window in which vegetation is

biochemically active and participating in gas exchange.

All phenocam indices overestimated starting dates of stabilization while underestimating onset of senescence yet there was considerable precision for these midseason metrics. For stable period onset, this was indicative that phenocam observed changes in both greenness levels and canopy structure that were occurring beyond when peak ecosystem net productivity rates were achieved. Maximum rates of increasing amplitude were lower in most indices, further supporting that maximum NEP is achived before vegetation reflectance becomes stable. Another possibility is that ecosystem respiration ramps up during the midseason period driven by soil temperature or increased root exudates and substrate availability of soil organic carbon (SOC; Hu et al., 2020; Trifunovic et al., 2020), effectively masking any further productivity increase as vegetation reaches maturity. Correspondingly, for senescence onset, phenocam observed both pigmentation and canopy structural changes occurring before the steady decline in net productivity. One possibility for this discrepancy is degradation within upper canopy leaves while subcanopy vegetation continues at near stable period productivity rates. Although recognized as an issue in forested systems (Ahl et al., 2006), it suggests that even when dealing with a relatively short canopy, more information could be required about subcanopy conditions. It is important to recognize that NEP measured with the EC technique essentially integrates all components of the canopy and misses potential lateral fluxes of carbon (Trifunovic et al., 2020), while spectral sensors focus primarily on top of canopy reflectance information (Dechant et al., 2020).

During midseason periods, greenness (proxy for chlorophyll pigmentation and photosynthetic capacity) and structural changes are more in sync as observed by phenocam. In regard to NEP, this is reflected as a midseason plateau in most ecosystems where daily rates of NEP hold steady (i.e., stable period) (Gu et al., 2009). Midseason phenology dates derived from phenocam visible wavelength indices and infrared bands showed similarities between years, within 13 and 9 days for 2017 and 2018 stabilization dates and within 12 and 6 days for 2017 and 2018 downturn dates, respectively. This indicates that during the stable period of sustained maximum net productivity the canopy likely tends to optimize structure for functionality and just as equally, optimizes functionality from structure. This is especially the case in highly clonal stands where individual and canopy optimization goals are more aligned (Anten, 2004). These findings are supported by the Monsi–Saeki theory which states plant canopies will tend towards an optimal structure (LAI, leaf angle, density) to maximize photosynthetic efficiency and in stands with little or no interspecific competition, such as a salt marsh, the optimum structure-function relationship is more attainable (Hirose, 2005).

4.3. SRS and MODIS carbon phenology transition dates

Primary indices from SRS sensors (NDVI) and MODIS-derived indices (NDVI and EVI) underpredict start and overpredict end of carbon sink season while midseason metrics are inconsistent. This results in overpredictions of carbon sink season length. We emphasize that a combination of ecosystem specific factors (e.g., aerenchyma, exposed sediments, elevated soil moisture, dead vegetation) likely introduce discrepancies with indices incorporating infrared reflectance. MODIS-derived indices had larger offsets compared to SRS sensors which is likely the combined result of vastly different viewing footprints (250km vs. ~9m), temporal resolution (16-day vs daily), spectral bandwidth differences (SRS sensors have narrower bandwidth; Table 1) and orientation angles. Phenological information extracted from MODIS MOD13Q1 product requires interpolation which can fail to accurately capture periods of rapid change (Rankine et al., 2017). SRS sensors showed improvements, but results were inconsistent due to increased reflectance scattering in infrared bandwidths. At our site, SRS sensors are positioned with a larger downward angle from the horizontal, thus there is potential for greater interference from sediment and water backgrounds (especially under flooded conditions). While SRS NIRv provided improvement as it was designed to minimize non-vegetation infrared signals, lingering infrared reflectance in late 2018 caused discrepancies. Midseason metrics were characterized by inconsistencies in both sensors although patterns were evident. Mainly under prediction of stabilization and over prediction of downturn which was the opposite trend of phenocam. The shift was greater for downturn indicating end of season discrepancies were beginning to develop earlier than phenocam. This may indicate that changes in reflectance spurred by intermixed living and dead vegetation occurs more rapidly with sharper sensor angles within the relatively narrow bandwidths of SRS and MODIS while phenocam response was more mediated by larger viewing fields, oblique orientation and wider spectral bandwidths. Although MODIS products are commonplace in parameterizing earth system models, other less utilized satellite products could prove better and should be considered in future studies (i.e., Landsat and Sentinel products; Kowalski et al., 2020).

4.4. Daily net productivity tracking using spectral reflectance

All sensors and vegetation indices tracked daily NEP with moderately strong correlations but visible wavelength indices and NDVI from phenocam provided best fits. This resulted from tight coupling between spring and fall time VI-NEP relationships. Other indices which included an infrared band had higher degrees of separation which generated a seasonal hysteresis pattern where springtime reflectance values were associated with higher NEP compared to fall. Although the overall fit for phenocam NDVI was high ($R^2 = 0.87$) it was not devoid of this spring-fall mismatch. The description of this phenomenon is lacking in salt-marsh literature yet has been documented for relationships between NDVI and fraction of absorbed PAR in grassland (Flanagan et al., 2015; Wang et al., 2020), cropland (Gitelson et al., 2014; Peng et al., 2017), and deciduous broadleaf forests (Muraoka et al., 2013). This is likely a plausible phenomenon generated by physiological declines in efficiency of photosynthetic machinery and CO_2 harvesting enzymes during fall months, resultant from photooxidation effects accumulated over the growing season (Liu et al., 2019). This assertion is supported by considerably lower light saturation levels (~1000 μmols) compared to typical C4 plants (Kathilankal et al., 2011), where vegetation is subjected to saturating levels for most of the growth cycle which increases photosystem stress and places demand on non-photochemical quenching processes. Thus, phenocam NDVI appears to give more detail in context of seasonality while providing linear fits comparable to visible wavelength indices.

It was evident that some VI-NEP relationships, mainly NDVI from SRS and MODIS, appear to follow an exponential fit. While implementing this provided slight improvements ($R^2 = 0.85$ linear vs. $R^2 = 0.89$ exponential for SRS NDVI) ($R^2 = 0.87$ linear vs $R^2 = 0.90$ exponential for MODIS NDVI), the responses were identical for phenocam ($R^2 = 0.90$). This could indicate tendency for saturation at higher reflectance values with SRS and MODIS which use narrower red full width half maximum bandwidths (10 and 50 nm, respectively) compared to phenocam (135 nm). We highlight that phenocam is the only sensor with spectral overlap which extends into infrared and red edge spectral regions (680–750nm) (Horler et al., 1983), whereas SRS sensors have relatively limited bandwidths (Gamon et al., 2015) and MODIS was engineered to very specific wavelengths to prevent atmospheric interference issues. This broadband capability allows phenocam NDVI to incorporate physiological information on chlorophyll content while relaying information on LAI and canopy structure (Brown et al., 2016; Rossi et al., 2019). This could explain why phenocam NDVI tracked daily NEP similar to visible wavelength indices yet generated large discrepancies by overestimating season end dates. Results of this study show that specific sensors and vegetation indices may be suited to different spatiotemporal applications such as subcanopy phenology profiles, species specific reflectance, delineating and parsing key regions of interest within an ecosystem and whole ecosystem coverage, but

within a salt marsh environment where soils and vegetation possesses unique physical properties, the phenocam offers a wide range of these applications while providing accurate daily tracking and phenoperiod predictions.

4.5. Proximal sensors vs MODIS

Differences between spatial domains showed disconnections with RED and NIR reflectance while primary indices had better agreement. Aside from spectral bandwidth discrepancies (mostly phenocam) there are two main differences between proximal and MODIS data: 1) viewing angle and acquisition interval; and 2) EC footprint-to-target-area mismatch. While longer acquisition intervals likely contributes to challenges of generating accurate phenology parameters it should be less problematic for general tracking. Our results suggest added effects from viewing angle discrepancies as the oblique view provided by proximal sensors (especially phenocam) captures canopy reflectance at an apparent higher vegetation density from increased stand overlap than does the nadir view provided by MODIS (Ryu et al., 2014). In this regard, MODIS will inherently have greater interference from exposed sediments and open water features. This should be especially relevant for dominate short form *Spartina* vegetation located on marsh platforms which is characterized by low leaf area and pronounced upright growth to minimize saturating levels of PAR. Finally, there is bias as a consequence of potential EC footprint-to-target-area mismatch (Chu et al., 2021). Our study site has high representativeness for a MODIS pixel of 250m but (as in most EC towers) this representativeness is reduced for target areas beyond 500 m. The combination of viewing angle, acquisition interval and footprint-to-target-area mismatch may explain larger offsets from MODIS predictions.

5. Conclusions

Our assessment of phenocam, SRS sensors and MODIS revealed that while daily tracking was excellent across sensors, the most widely used and accepted indices such as NDVI and EVI suffered discrepancies during start and end of season dates which resulted in overpredictions of season length. These over predictions were greatest from MODIS-derived indices and narrowband SRS sensors which introduced divergence in the flux-reflectance relationship, thus affecting accuracy for carbon modeling applications. Our results provide support for phenocam as the preferred method in terms of accuracy, available features, sampling footprint and versatility for a salt marsh where there is both interpretation and scaling challenges. Given the heterogeneities of the salt marsh, phenocam allows for consideration of a larger viewing footprint which integrates more of the processes observed by the flux tower. Available spectral channels and bandwidths allows for formulation of numerous indices that can provide insight into different aspects of ecosystem phenology including structural and functional changes with the added benefit of providing true color human viewable images. This feature can be leveraged to monitor site conditions while offering a friendly and familiar medium for citizen science opportunities and education. Additional benefits include support from the phenocam network on site-specific camera model selection, configuration, implementation and free long-term image data archiving.

While MODIS-derived indices have obvious advantages with respect to global coverage, serious limitations arise when dealing with an ecosystem that is spatially limited and confined to coastal interfaces. The impetus for global coverage cannot evade the need for remote sensing linkages, thus we need further studies which attempt to disentangle discrepancies introduced from standing dead biomass during dormancy and the mix of dead and living vegetation during spring and (especially) fall transitional periods. We need to look more closely at special conditions such as how changes in above ground aerenchyma tissues common to wetland/salt marsh vegetation affects the spectral response, how gradients in elevation and sediment moisture (as drivers of aerenchyma development and canopy structure) may affect heterogeneity of altered reflectance signals and how residual salts on leaf surfaces can modify reflectance. It will be equally important to incorporate longer timeseries to help test consistencies between sensors and indices and across other salt marshes. Ultimately, our ability to accurately characterize phenological cycles within the salt-marsh environment will help to improve modeling efforts as physiological parameters are not static, but rather dynamic in response to the interplay of annual climatic conditions, biophysical factors and site ecology. Phenology provides an effective method for tracking daily changes in ecosystem carbon exchange while enabling the binning of time periods to derive more dynamic modeling parameters.

Declaration of Competing Interest

The authors declare that they have no known competing financial interests or personal relationships that could have appeared to influence the work reported in this paper.

Acknowledgments

This study was supported by the National Science Foundation (#1652594). We thank the onsite support from the Delaware National Estuarine Research Reserve (DNERR). The authors acknowledge the land on which they realized this study as the traditional home of the Lenni-Lenape tribal nation (Delaware nation).

Supplementary materials

Supplementary material associated with this article can be found, in the online version, at doi:10.1016/j.agrformet.2021.108481.

References

Ahl, D.E., Gower, S.T., Burrows, S.N., Shabanov, N.V., Myneni, R.B., Knyazikhin, Y., 2006. Monitoring spring canopy phenology of a deciduous broadleaf forest using MODIS. Remote Sens. Environ. 104, 88–95.

Anten, N.P.R., 2004. Optimal photosynthetic characteristics of individual plants in vegetation stands and implications for species coexistence. Ann. Botany 95, 495–506.

Arriga, N., Rannik, Ü., Aubinet, M., Carrara, A., Vesala, T., Papale, D., 2017. Experimental validation of footprint models for eddy covariance CO2 flux measurements above grassland by means of natural and artificial tracers. Agric. For. Meteorol. 242, 75–84.

Aubinet, M., Vesala, T., Papale, D., 2012. Eddy Covariance: A Practical Guide to Measurement and Data Analysis. Springer Science & Business Media.

Badgley, G., Field, C.B., Berry, J.A., 2017. Canopy near-infrared reflectance and terrestrial photosynthesis. Sci. Adv. 3.

Baldocchi, D.D., 2003. Assessing the eddy covariance technique for evaluating carbon dioxide exchange rates of ecosystems: past, present and future. Glob. Change Biol. 9, 479–492.

Baldocchi, D.D., Ryu, Y., Dechant, B., Eichelmann, E., Hemes, K., Ma, S., Rey Sanchez, C., Shortt, R., Szutu, D., Valach, A., 2020. Outgoing near infrared radiation from vegetation scales with canopy photosynthesis across a spectrum of function, structure, physiological capacity and weather. J. Geophys. Res.: Biogeosci., e2019JG005534

Balzarolo, M., Vicca, S., Nguy-Robertson, A.L., Bonal, D., Elbers, J.A., Fu, Y.H., Grunwald, T., Horemans, J.A., Papale, D., Penuelas, J., Suyker, A., Veroustraete, F., 2016. Matching the phenology of net ecosystem exchange and vegetation indices estimated with MODIS and FLUXNET in-situ observations. Remote Sens. Environ. 174, 290–300.

Barbier, E.B., Hacker, S.D., Kennedy, C., Koch, E.W., Stier, A.C., Silliman, B.R., 2011. The value of estuarine and coastal ecosystem services. Ecol. Monogr. 81, 169–193.

Brown, T.B., Hultine, K.R., Steltzer, H., Denny, E.G., Denslow, M.W., Granados, J., Henderson, S., Moore, D., Nagai, S., SanClements, M., Sanchez-Azofeifa, A., Sonnentag, O., Tazik, D., Richardson, A.D., 2016. Using phenocams to monitor our changing Earth: toward a global phenocam network. Front. Ecol. Environ. 14, 84–93.

Cao, L., Zhou, Z., Xu, X., Shi, F., 2020. Spatial and temporal variations of the greenhouse gas emissions in coastal saline wetlands in southeastern China. Environ. Sci. Pollut. Res. 27, 1118–1130.

Capooci, M., Barba, J., Seyfferth, A.L., Vargas, R., 2019. Experimental influence of storm-surge salinity on soil greenhouse gas emissions from a tidal salt marsh. Sci. Total Environ. 686, 1164–1172.

Chu, H., Luo, X., Ouyang, Z., Chan, W.S., Dengel, S., Biraud, S.C., Torn, M.S., Metzger, S., Kumar, J., Arain, M.A., 2021. Representativeness of Eddy-Covariance flux footprints for areas surrounding AmeriFlux sites. Agric. For. Meteorol. 301, 108350.

Colmer, T.D., Flowers, T.J., 2008. Flooding tolerance in halophytes. New Phytol. 179, 964–973.
Courtney, A.J., Xu, J.C., Xu, Y., 2016. Responses of growth, antioxidants and gene expression in smooth cordgrass (Spartina alterniflora) to various levels of salinity. Plant Physiol. Biochem. 99, 162–170.
Dechant, B., Ryu, Y., Badgley, G., Zeng, Y., Berry, J.A., Zhang, Y., Goulas, Y., Li, Z., Zhang, Q., Kang, M., Li, J., Moya, I., 2020. Canopy structure explains the relationship between photosynthesis and sun-induced chlorophyll fluorescence in crops. Remote Sens. Environ. 241, 111733.
Dian, Y., Le, Y., Fang, S., Xu, Y., Yao, C., Liu, G., 2016. Influence of spectral bandwidth and position on chlorophyll content retrieval at leaf and canopy levels. J. Indian Soc. Remote Sens. 44, 583–593.
Dronova, I., Taddeo, S., Hemes, K.S., Knox, S.H., Valach, A., Oikawa, P.Y., Kasak, K., Baldocchi, D.D., 2021. Remotely sensed phenological heterogeneity of restored wetlands: linking vegetation structure and function. Agric. For. Meteorol. 296, 108215.
Fatichi, S., Pappas, C., Zscheischler, J., Leuzinger, S., 2019. Modelling carbon sources and sinks in terrestrial vegetation. New Phytol. 221, 652–668.
Feagin, R., Forbrich, I., Huff, T., Barr, J., Ruiz-Plancarte, J., Fuentes, J., Najjar, R., Vargas, R., Vázquez-Lule, A., Windham-Myers, L., 2020. Tidal wetland gross primary production across the continental United States, 2000–2019. Glob. Biogeochem. Cycles 34, e2019GB006349.
Filippa, G., Cremonese, E., Migliavacca, M., Galvagno, M., Forkel, M., Wingate, L., Tomelleri, E., di Cella, U.M., Richardson, A.D., 2016. Phenopix: a R package for image-based vegetation phenology. Agric. Forest Meteorol. 220, 141–150.
Filippa, G., Cremonese, E., Migliavacca, M., Galvagno, M., Sonnentag, O., Humphreys, E., Hufkens, K., Ryu, Y., Verfaillie, J., di Cella, U.M., Richardson, A.D., 2018. NDVI derived from near-infrared-enabled digital cameras: applicability across different plant functional types. Agric. For. Meteorol. 249, 275–285.
Flanagan, L.B., Sharp, E.J., Gamon, J.A., 2015. Application of the photosynthetic light-use efficiency model in a northern Great Plains grassland. Remote Sens. Environ. 168, 239–251.
Foroughi, H., Naseri, A.A., Boroomand Nasabm, S., Hamzeh, S., Sadeghi, M., Tuller, M., Jones, S.B., 2020. A new mathematical formulation for remote sensing of soil moisture based on the Red-NIR space. Int. J. Remote Sens. 41, 8034–8047.
Forbrich, I., Giblin, A.E., 2015. Marsh-atmosphere CO_2 exchange in a New England salt marsh. J. Geophys. Res.: Biogeosci. 120, 1825–1838.
Forkel, M., Migliavacca, M., Thonicke, K., Reichstein, M., Schaphoff, S., Weber, U., Carvalhais, N., 2015. Codominant water control on global interannual variability and trends in land surface phenology and greenness. Glob. Change Biol. 21, 3414–3435.
Gamon, J.A., 2015. Reviews and syntheses: optical sampling of the flux tower footprint. Biogeosciences 12, 4509–4523.
Gamon, J.A., Kovalchuck, O., Wong, C.Y.S., Harris, A., Garrity, S.R., 2015. Monitoring seasonal and diurnal changes in photosynthetic pigments with automated PRI and NDVI sensors. Biogeosciences 12, 4149–4159.
Garbulsky, M.F., Penuelas, J., Gamon, J., Inoue, Y., Filella, I., 2011. The photochemical reflectance index (PRI) and the remote sensing of leaf, canopy and ecosystem radiation use efficiencies: a review and meta-analysis. Remote Sens. Environ. 115, 281–297.
Garrity, S.R., Bohrer, G., Maurer, K.D., Mueller, K.L., Vogel, C.S., Curtis, P.S., 2011. A comparison of multiple phenology data sources for estimating seasonal transitions in deciduous forest carbon exchange. Agric. For. Meteorol. 151, 1741–1752.
Ghosh, S., Mishra, D., 2017. Analyzing the long-term phenological trends of salt marsh ecosystem across coastal Louisiana. Remote Sens. 9, 1340.
Ghulam, A., Qin, Q.M., Teyip, T., Li, Z.L., 2007. Modified perpendicular drought index (MPDI): a real-time drought monitoring method. ISPRS J. Photogramm. Remote Sens. 62, 150–164.
Gitelson, A.A., Peng, Y., Huemmrich, K.F., 2014. Relationship between fraction of radiation absorbed by photosynthesizing maize and soybean canopies and NDVI from remotely sensed data taken at close range and from MODIS 250 m resolution data. Remote Sens. Environ. 147, 108–120.
Gu, L., Post, W.M., Baldocchi, D.D., Black, T.A., Suyker, A.E., Verma, S.B., Vesala, T., Wofsy, S.C., 2009. Characterizing the seasonal dynamics of plant community photosynthesis across a range of vegetation types. Phenol. Ecosyst. Process. 35–58. Springer.
Helman, D., 2018. Land surface phenology: what do we really 'see' from space? Sci. Total Environ. 618, 665–673.
Himes-Cornell, A., Pendleton, L., Atiyah, P., 2018. Valuing ecosystem services from blue forests: a systematic review of the valuation of salt marshes, sea grass beds and mangrove forests. Ecosyst. Serv. 30, 36–48.
Hirose, T., 2005. Development of the Monsi–Saeki theory on canopy structure and function. Ann. Botany 95, 483–494.
Hmimina, G., Dufrene, E., Pontailler, J.Y., Delpierre, N., Aubinet, M., Caquet, B., de Grandcourt, A., Burban, B., Flechard, C., Granier, A., Gross, P., Heinesch, B., Longdoz, B., Moureaux, C., Ourcival, J.M., Rambal, S., Saint Andre, L., Soudani, K., 2013. Evaluation of the potential of MODIS satellite data to predict vegetation phenology in different biomes: an investigation using ground-based NDVI measurements. Remote Sens. Environ. 132, 145–158.
Horler, D.N.H., Dockray, M., Barber, J., 1983. The red edge of plant leaf reflectance. Int. J. Remote Sens. 4, 273–288.
Huang, T., Liang, L., Wang, J., Geng, D., Luo, X., Wang, L., 2019. Influence of vegetation index on LAI inversion accuracy at different bandwidths. In: Proceedings of the 8th International Conference on Agro-Geoinformatics (Agro-Geoinformatics), pp. 1–6.
Hu, M.J., Sardans, J., Yang, X.Y., Penuelas, J., Tong, C., 2020. Patterns and environmental drivers of greenhouse gas fluxes in the coastal wetlands of China: a systematic review and synthesis. Environ. Res. 186, 10.
Jiang, Z., Huete, A.R., Didan, K., Miura, T., 2008. Development of a two-band enhanced vegetation index without a blue band. Remote Sens. Environ. 112, 3833–3845.
Kathilankal, J.C., Mozdzer, T.J., Fuentes, J.D., McGlathery, K.J., D'Odorico, P., Zieman, J.C., 2011. Physiological responses of Spartina alterniflora to varying environmental conditions in Virginia marshes. Hydrobiologia 669, 167.
Keenan, T.F., Darby, B., Felts, E., Sonnentag, O., Friedl, M.A., Hufkens, K., O'Keefe, J., Klosterman, S., Munger, J.W., Toomey, M., Richardson, A.D., 2014. Tracking forest phenology and seasonal physiology using digital repeat photography: a critical assessment. Ecol. Appl. 24, 1478–1489.
Kljun, N., Calanca, P., Rotach, M.W., Schmid, H.P., 2004. A simple parameterisation for flux footprint predictions. Boundary-Layer Meteorology 112, 503–523.
Knox, S.H., Dronova, I., Sturtevant, C., Oikawa, P.Y., Matthes, J.H., Verfaillie, J., Baldocchi, D., 2017. Using digital camera and Landsat imagery with eddy covariance data to model gross primary production in restored wetlands. Agric. For. Meteorol. 237, 233–245.
Knox, S.H., Windham-Myers, L., Anderson, F., Sturtevant, C., Bergamaschi, B., 2018. Direct and indirect effects of tides on ecosystem-scale CO_2 exchange in a brackish tidal marsh in northern California. J. Geophys. Res.: Biogeosci. 123, 787–806.
Kowalski, K., Senf, C., Hostert, P., Pflugmacher, D., 2020. Characterizing spring phenology of temperate broadleaf forests using Landsat and Sentinel-2 time series. Int. J. Appl. Earth Obs. Geoinf. 92, 102172.
Liu, H.Q., Huete, A., 1995. A feedback based modification of the NDVI to minimize canopy background and atmospheric noise. IEEE Trans. Geosci. Remote Sens. 33, 457–465.
Liu, J., Lu, Y., Hua, W., Last, R.L., 2019. A new light on photosystem II maintenance in oxygenic photosynthesis. Front. Plant Sci. 10, 975-975.
Maleki, M., Arriga, N., Barrios, J.M., Wieneke, S., Liu, Q., Peñuelas, J., Janssens, I.A., Balzarolo, M., 2020. Estimation of gross primary productivity (GPP) phenology of a short-rotation plantation using remotely sensed indices derived from sentinel-2 images. Remote Sens. 12, 2104.
Maricle, B.R., Lee, R.W., 2002. Aerenchyma development and oxygen transport in the estuarine cordgrasses *Spartina alterniflora* and *S. anglica*. Aquat. Botany 74, 109–120.
McLeod, E., Chmura, G.L., Bouillon, S., Salm, R., Bjork, M., Duarte, C.M., Lovelock, C.E., Schlesinger, W.H., Silliman, B.R., 2011. A blueprint for blue carbon: toward an improved understanding of the role of vegetated coastal habitats in sequestering CO_2. Front. Ecol. Environ. 9, 552–560.
McOwen, C.J., Weatherdon, L.V., Bochove, J.W.V., Sullivan, E., Blyth, S., Zockler, C., Stanwell-Smith, D., Kingston, N., Martin, C.S., Spalding, M., Fletcher, S., 2017. A global map of saltmarshes. Biodiversity Data J. e11764-e11764.
Meier, R., Davin, E.L., Lejeune, Q., Hauser, M., Li, Y., Martens, B., Schultz, N.M., Sterling, S., Thiery, W., 2018. Evaluating and improving the Community Land Model's sensitivity to land cover. Biogeosciences 15, 4757.
Migliavacca, M., Galvagno, M., Cremonese, E., Rossini, M., Meroni, M., Sonnentag, O., Cogliati, S., Manca, G., Diotri, F., Busetto, L., Cescatti, A., Colombo, R., Fava, F., di Celia, U.M., Pari, E., Siniscalco, C., Richardson, A.D., 2011. Using digital repeat photography and eddy covariance data to model grassland phenology and photosynthetic CO_2 uptake. Agric. For. Meteorol. 151, 1325–1337.
Mo, Y., Momen, B., Kearney, M.S., 2015. Quantifying moderate resolution remote sensing phenology of Louisiana coastal marshes. Ecol. Model. 312, 191–199.
Moffett, K.B., Wolf, A., Berry, J.A., Gorelick, S.M., 2010. Salt marsh–atmosphere exchange of energy, water vapor, and carbon dioxide: effects of tidal flooding and biophysical controls. Water Resour. Res. 46.
Muraoka, H., Noda, H.M., Nagai, S., Motohka, T., Saitoh, T.M., Nasahara, K.N., Saigusa, N., 2013. Spectral vegetation indices as the indicator of canopy photosynthetic productivity in a deciduous broadleaf forest. J. Plant Ecol. 6, 393–407.
Murray, F.W., 1967. On the computation of saturation vapor pressure. J. Appl. Meteorol. Climatol. 6, 203–204.
Negandhi, K., Edwards, G., Kelleway, J.J., Howard, D., Safari, D., Saintilan, N., 2019. Blue carbon potential of coastal wetland restoration varies with inundation and rainfall. Sci. Rep. 9, 4368.
O'Connell, J.L., Alber, M., Pennings, S.C., 2020. Microspatial differences in soil temperature cause phenology change on par with long-term climate warming in salt marshes. Ecosystems 23, 498–510.
O'Connell, J.L., Mishra, D.R., Cotton, D.L., Wang, L., Alber, M., 2017. The Tidal Marsh Inundation Index (TMII): an inundation filter to flag flooded pixels and improve MODIS tidal marsh vegetation time-series analysis. Remote Sens. Environ. 201, 34–46.
Ollinger, S.V., 2011. Sources of variability in canopy reflectance and the convergent properties of plants. New Phytol. 189, 375–394.
Peng, Y., Nguy-Robertson, A., Arkebauer, T., Gitelson, A.A., 2017. Assessment of canopy chlorophyll content retrieval in maize and soybean: implications of hysteresis on the development of generic algorithms. Remote Sens. 9, 18.
Petach, A.R., Toomey, M., Aubrecht, D.M, Richardson, A.D., 2014. Monitoring vegetation phenology using an infrared-enabled security camera. Agric. For. Meteorol. 195-196, 143–151.
Peterson, P.M., Romaschenko, K., Arrieta, Y.H., Saarela, J.M., 2014. A molecular phylogeny and new subgeneric classification of Sporobolus (Poaceae: Chloridoideae: *Sporobolinae*). Taxon 63, 1212–1243.
Pham, T.D., Xia, J.S., Ha, N.T., Bui, D.T., Le, N.N., Takeuchi, W., 2019. A review of remote sensing approaches for monitoring blue carbon ecosystems: mangroves, seagrasses and salt marshes during 2010-2018. Sensors 19, 37.

Piao, S., Liu, Q, Chen, A., Janssens, I.A., Fu, Y., Dai, J., Liu, L., Lian, X., Shen, M., Zhu, X., 2019. Plant phenology and global climate change: current progresses and challenges. Glob. Change Biol. 25, 1922–1940.
Rankine, C., Sanchez-Azofeifa, G.A., Guzman, J.A., Espirito-Santo, M.M., Sharp, I., 2017. Comparing MODIS and near-surface vegetation indexes for monitoring tropical dry forest phenology along a successional gradient using optical phenology towers. Environ. Res. Lett. 12, 15.
Ren, H., Zhou, G., 2019. Estimating green biomass ratio with remote sensing in arid grasslands. Ecol. Indic. 98, 568–574.
Richardson, A.D., Braswell, B.H., Hollinger, D.J., Jenkins, J.P., Ollinger, S.V., 2009. Near-surface remote sensing of spatial and temporal variation in canopy phenology. Ecol. Appl. 19, 1417–1428.
Richardson, A.D., Keenan, T.F., Migliavacca, M., Ryu, Y., Sonnentag, O., Toomey, M., 2013. Climate change, phenology, and phenological control of vegetation feedbacks to the climate system. Agric. For. Meteorol. 169, 156–173.
Rocha, A.V., Potts, D.L., Goulden, M.L., 2008. Standing litter as a driver of interannual CO_2 exchange variability in a freshwater marsh. J. Geophys. Res.: Biogeosci. 113.
Rossi, M., Niedrist, G., Asam, S., Tonon, G., Tomelleri, E., Zebisch, M., 2019. A comparison of the signal from diverse optical sensors for monitoring alpine grassland dynamics. Remote Sens. 11, 22.
Ryu, Y., Lee, G., Jeon, S., Song, Y., Kimm, H., 2014. Monitoring multi-layer canopy spring phenology of temperate deciduous and evergreen forests using low-cost spectral sensors. Remote Sens. Environ. 149, 227–238.
Sapkota, Y., White, J.R., 2020. Carbon offset market methodologies applicable for coastal wetland restoration and conservation in the United States: a review. Sci. Total Environ. 701, 9.
Seyednasrollah, B., Young, A.M., Hufkens, K., Milliman, T., Friedl, M.A., Frolking, S., Richardson, A.D., 2019. Tracking vegetation phenology across diverse biomes using Version 2.0 of the PhenoCam Dataset. Sci. Data 6.
Seyednasrollah, B., 2018. Hazer: Quantifying Haze Factor for RGB Images to Identify Cloudy and Foggy Weather. R package version 1.1.1, http://doi.org/10.5281/zenodo.1008568.
Seyfferth, A.L., Bothfeld, F., Vargas, R., Stuckey, J.W., Wang, J., Kearns, J., Michael, H. A., Guimond, J., Yu, X., Sparks, D.L., 2020. Spatial and temporal heterogeneity of geochemical controls on carbon cycling in a tidal salt marsh. Geochim. Cosmochim. Acta 282, 1–18.
Slaton, M.R., Hunt, E.R., Smith, W.K., 2001. Estimating near-infrared leaf reflectance from leaf structural characteristics. Am. J. Botany 88, 278–284.
Sonnentag, O., Hufkens, K., Teshera-Sterne, C., Young, A.M., Friedl, M., Braswell, B.H., Milliman, T., O'Keefe, J., Richardson, A.D., 2012. Digital repeat photography for phenological research in forest ecosystems. Agric. For. Meteorol. 152, 159–177.
eds. Sorrell, B.K., Brix, H., 2013. Gas transport and exchange through wetland plant aerenchyma. In: DeLaune, R.D., Reddy, K.R., Richardson, C.J., Megonigal, J.P. (Eds.), Methods in Biogeochemistry of Wetlands. Soil Science Soc Amer, Madison, pp. 177–196. eds.
St Peter, J., Hogland, J., Hebblewhite, M., Hurley, M.A., Hupp, N., Proffitt, K., 2018. Linking phenological indices from digital cameras in Idaho and Montana to MODIS NDVI. Remote Sens. 10.
Taddeo, S., Dronova, I., Depsky, N., 2019. Spectral vegetation indices of wetland greenness: responses to vegetation structure, composition, and spatial distribution. Remote Sens. Environ. 234, 111467.
Tang, J., Ye, S., Chen, X., Yang, H., Sun, X., Wang, F., Wen, Q., Chen, S., 2018. Coastal blue carbon: concept, study method, and the application to ecological restoration. Sci. China Earth Sci. 61, 637–646.
Tong, C., Wang, W.Q., Huang, J.F., Gauci, V., Zhang, L.H., Zeng, C.S., 2012. Invasive alien plants increase CH_4 emissions from a subtropical tidal estuarine wetland. Biogeochemistry 111, 677–693.
Trifunovic, B., Vázquez-Lule, A., Capooci, M., Seyfferth, A.L., Moffat, C., Vargas, R., 2020. Carbon dioxide and methane emissions from temperate salt marsh tidal creek. J. Geophys. Res.: Biogeosci. 125, 84.
Vázquez-Lule, A., Colditz, R., Herrera-Silveira, J., Guevara, M., Rodríguez-Zúñiga, M.T., Cruz, I., Ressl, R., Vargas, R., 2019. Greenness trends and carbon stocks of mangroves across Mexico. Environ. Res. Lett. 14, 075010.
Vázquez-Lule, A., Vargas, R., 2021. Biophysical drivers of net ecosystem and methane exchange across phenological phases in a tidal salt marsh. Agric. For. Meteorol. 300, 108309.
Wang, R., Gamon, J.A., Emmerton, C.A., Springer, K.R., Yu, R., Hmimina, G., 2020. Detecting intra- and inter-annual variability in gross primary productivity of a North American grassland using MODIS MAIAC data. Agric. For. Meteorol. 281, 12.
Ward, N.D., Megonigal, J.P., Bond-Lamberty, B., Bailey, V.L., Butman, D., Canuel, E.A., Diefenderfer, H., Ganju, N.K., Goñi, M.A., Graham, E.B., Hopkinson, C.S., Khangaonkar, T., Langley, J.A., McDowell, N.G., Myers-Pigg, A.N., Neumann, R.B., Osburn, C.L., Price, R.M., Rowland, J., Sengupta, A., Simard, M., Thornton, P.E., Tzortziou, M., Vargas, R., Weisenhorn, P.B., Windham-Myers, L., 2020. Representing the function and sensitivity of coastal interfaces in Earth system models. Nat. Commun. 11, 2458.
Wei, S., Han, G., Jia, X., Song, W., Chu, X., He, W., Xia, J., Wu, H., 2020. Tidal effects on ecosystem CO_2 exchange at multiple timescales in a salt marsh in the Yellow River Delta. Estuarine. Coast. Shelf Sci. 238, 106727.
Weston, N.B., Neubauer, S.C., Velinsky, D.J., Vile, M.A., 2014. Net ecosystem carbon exchange and the greenhouse gas balance of tidal marshes along an estuarine salinity gradient. Biogeochemistry 120, 163–189.
Woolley, J.T., 1971. Reflectance and transmittance of light by leaves. Plant Physiol. 47, 656–662.
Wu, C., 2012. Use of a vegetation index model to estimate gross primary production in open grassland. J. Appl. Remote Sens. 6, 063532.
Xu, D.D., Guo, X.L., Li, Z.Q., Yang, X.H., Yin, H., 2014. Measuring the dead component of mixed grassland with Landsat imagery. Remote Sens. Environ. 142, 33–43.
Yan, D., Scott, R., Moore, D., Biederman, J., Smith, W., 2019. Understanding the relationship between vegetation greenness and productivity across dryland ecosystems through the integration of PhenoCam, satellite, and eddy covariance data. Remote Sens. Environ. 223, 50–62.
Yuan, W.P., Liu, S.G., Yu, G.R., Bonnefond, J.M., Chen, J.Q., Davis, K., Desai, A.R., Goldstein, A.H., Gianelle, D., Rossi, F., Suyker, A.E., Verma, S.B., 2010. Global estimates of evapotranspiration and gross primary production based on MODIS and global meteorology data. Remote Sens. Environ. 114, 1416–1431.
Zhang, X.Y., Jayavelu, S., Liu, L.L., Friedl, M.A., Henebry, G.M., Liu, Y., Schaaf, C.B., Richardson, A.D., Gray, J., 2018. Evaluation of land surface phenology from VIIRS data using time series of PhenoCam imagery. Agric. For. Meteorol. 256, 137–149.
Zhao, B., Donnelly, A., Schwartz, M.D., 2020. Evaluating autumn phenology derived from field observations, satellite data, and carbon flux measurements in a northern mixed forest, USA. Int. J. Biometeorol. 1–15.
Zhu, X.D., Meng, L.X., Zhang, Y.H., Weng, Q.H., Morris, J., 2019. Tidal and meteorological influences on the growth of invasive Spartina alterniflora: evidence from UAV remote sensing. Remote Sens. 11.
Zhu, Z., Piao, S., Myneni, R.B., Huang, M., Zeng, Z., Canadell, J.G., Ciais, P., Sitch, S., Friedlingstein, P., Arneth, A., Cao, C., Cheng, L., Kato, E., Koven, C., Li, Y., Lian, X., Liu, Y., Liu, R., Mao, J., Pan, Y., Peng, S., Peñuelas, J., Poulter, B., Pugh, T.A.M., Stocker, B.D., Viovy, N., Wang, X., Wang, Y., Xiao, Z., Yang, H., Zaehle, S., Zeng, N., 2016. Greening of the Earth and its drivers. Nat. Clim. Change 6, 791–795.
Kormann, R., Meixner, F.X., 2001. An analytical footprint model for non-neutral stratification. Boundary-Layer Meteorology, 99, 207–224.